Theoretical study on rotary-sliding disk triboelectric nanogenerators in contact and non-contact modes

Tao Jiang[1,§], Xiangyu Chen[1,§], Keda Yang[2], Changbao Han[1], Wei Tang[1], and Zhong Lin Wang[1,3] (✉)

[1] *Beijing Institute of Nanoenergy and Nanosystems, Chinese Academy of Sciences, Beijing 100083, China*

[2] *Computer Network Information Center, Chinese Academy of Sciences, Beijing 100190, China*

[3] *School of Materials Science and Engineering, Georgia Institute of Technology, Atlanta, GA 30332-0245, USA*

[§] *These authors contributed equally to this work.*

ABSTRACT

The triboelectric nanogenerator (TENG) has emerged as a new and effective mechanical energy harvesting technology. In this work, a theoretical model for a rotary-sliding disk TENG with grating structure was constructed, including the dielectric-to-dielectric and conductor-to-dielectric cases. The finite element method (FEM) was utilized to characterize the fundamental physics of the rotary-sliding disk TENG working in both contact and non-contact modes. The basic properties of disk TENG were found to be controlled by the structural parameters such as tribo-surface spacing, grating number, and geometric size. From the FEM calculations, an approximate $V–Q–\alpha$ relationship was built through the interpolation method, and then the TENG dynamic output characteristics with arbitrary load resistance were numerically calculated. Finally, the dependencies of output power and matched resistance on the structural parameters and rotation rate were revealed. The present work provides an in-depth understanding of the working principle of the rotary-sliding disk TENG and serves as important guidance for optimizing TENG output performance in specific applications.

1 Introduction

A rapidly growing global demand for energy supply has spurred considerable interest in harvesting energy from the ambient environment [1–4]. Traditional mechanical energy harvesting is based on technologies such as piezoelectrics [5, 6], electromagnetics [7, 8], and electrostatics [9, 10]. Recently, the invention of triboelectric nanogenerators (TENGs) has provided an effective approach to convert mechanical energy into electricity based on the coupling effect of triboelectrification and electrostatic induction [11–14]. TENGs exhibit unique merits including high output power, low weight and fabrication cost, and high efficiency [15, 16]. For two basic modes of TENG, relative to the contact mode, the sliding mode is much easier for fully packaging and more effective for static charge generation [17, 18]. The rotary-sliding disk

TENG (RD-TENG) with a micro-sized grating structure has also been developed recently [19–21]. This design facilitates a rotation-induced periodic, in-plane charge separation for electricity generation. In our previous work, innovative rotation-based TENG devices were fabricated, and the measurements of electric output showed that both finer segmentations and larger rotation rate lead to a faster charge transfer between the electrodes through an external circuit, producing a large current output at a high frequency [19]. In addition, we utilized the disk-shaped design to simulate the braking system in an automobile, and found its practical applications in harvesting rotational energies [20]. Nevertheless, so far a systematic theoretical model for the RD-TENG is still lacking, and the issue of how the structural parameters and operating conditions of RD-TENG affect the match with the load remains to be studied, which is critical for performance improvement.

In the present work, theoretical models of two categories of rotary-sliding disk TENG with a grating structure are discussed in detail; each of them has contact and non-contact modes. We adopted the finite element method (FEM) to calculate the basic properties of RD-TENG and investigate the impacts of tribo-surface spacing, grating number, and geometric size of the TENG on its output. On the basis of the FEM results, an approximate governing equation was obtained with the continuous fraction interpolation method, and the TENG real-time output characteristics were mathematically calculated for both the dielectric-to-dielectric and conductor-to-dielectric cases. Finally, the influences of structural parameters and rotation rate on the average output power are addressed and power optimization strategies are provided.

2 Fundamental physics of rotary-sliding disk TENG

The rotary-sliding disk TENG has two types: dielectric-to-dielectric and conductor-to-dielectric, according to the materials of the triboelectric layers. The FEM models for the dielectric-to-dielectric and conductor-to-dielectric categories of TENG (denoted by dielectric RD-TENG and metal RD-TENG) with a grating structure were constructed as shown in Figs. 1(a) and 1(b).

For either category, the TENG possesses two working modes, i.e., the contact and non-contact mode, where the tribo-surface spacing h is zero and nonzero, respectively. In the 3D models, the dimensions are close to those of real devices. For dielectric RD-TENG, two grating-structured metal electrodes with a thickness of 0.01 mm are attached by two dielectric layers (a thickness of 0.1 mm, represented by d_1 and d_2) with the same grating. The relative permittivities of dielectric 1 and dielectric 2 were chosen as $\varepsilon_{r1} = 4$ and $\varepsilon_{r2} = 2$. The bottom part acts as the stator, and the top part can rotate clockwise around the central axis of the TENG (the rotation angle is represented by α). The definitions of center angle θ_0 of the grating unit ($\theta_0 = \pi/N$, N is the grating number), and the inner and outer radius of the TENG (denoted by r_1 and r_2) are also shown in the schematic models. The detailed calculation parameters are listed in Table 1. When two dielectric layers are in contact, the charge densities at the lower surface of dielectric 1 and upper surface of dielectric 2 were assigned as $+\sigma$ and $-\sigma$ at the non-overlapped region, whereas uniform tribo-charges with the same density are distributed on the whole tribo-surfaces in the non-contact mode. For metal RD-TENG, the rotator consists of a metal layer only, and the top metal has the same amount of positive charges in total as the bottom dielectrics due to the charge conservation.

FEM simulations were carried out using COMSOL software under the short-circuit (SC) and open-circuit (OC) conditions. Taking the dielectric RD-TENG for instance, the calculation method of basic properties is described here. The metal units in each electrode group were assigned with the same electric potential to reflect the external connection. At the initial state, the top triboelectric dielectric layer is placed to overlap with dielectric 2 for the contact mode and match with dielectric 2 for the non-contact mode. The total charge on metal 1 is $-Q - Q_{initial}$ and that on metal 2 is $Q + Q_{initial}$, in which $Q_{initial}$ is the equilibrium charge level at the initial state and Q is the amount of transferred charges at a certain rotation angle α. For the contact mode, the tribo-charges on the overlapped tribo-surfaces can be regarded as 0 because the distance between the centers of positive and negative charges is at the atomic level; thus the $Q_{initial}$ is zero. However,
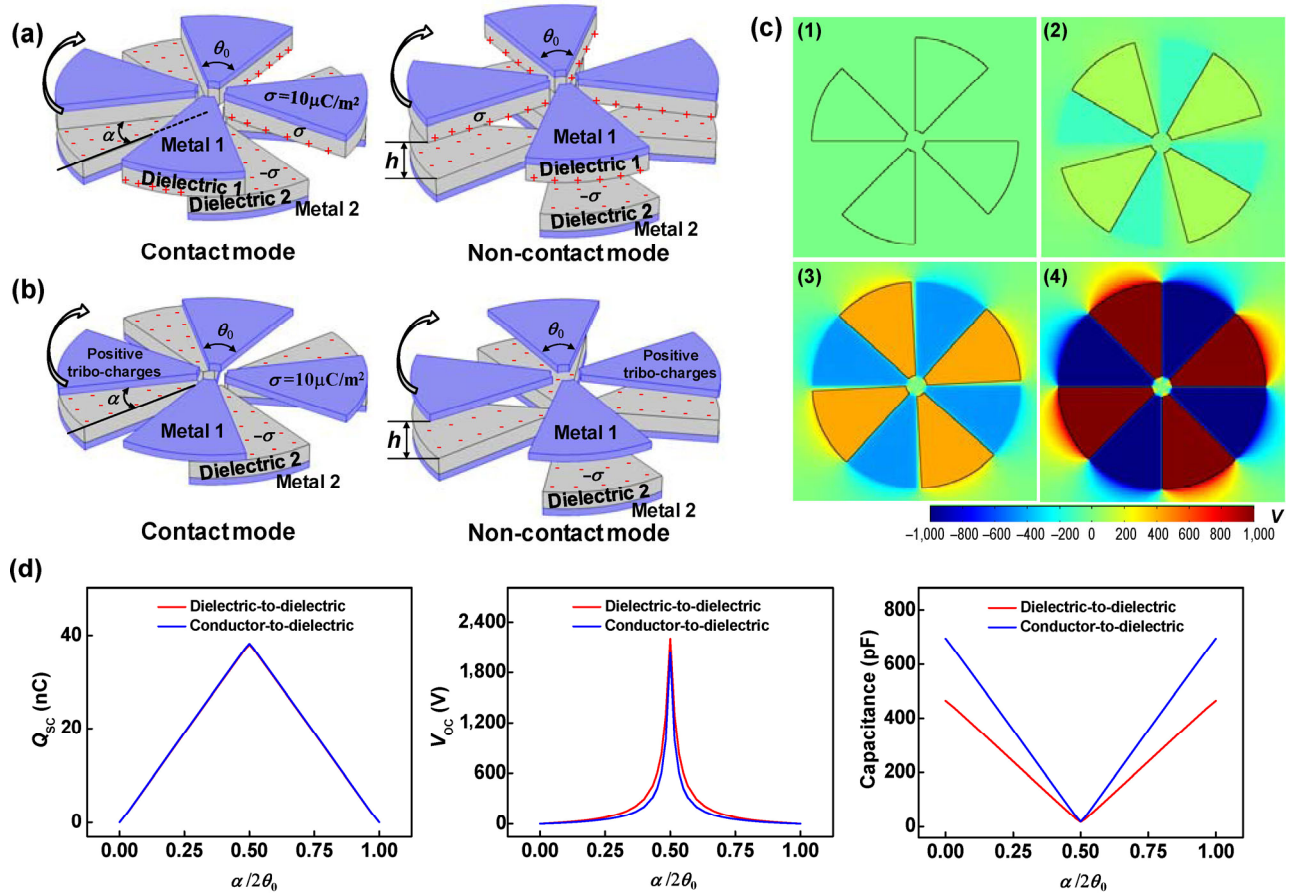
Figure 1 Model and basic properties of the TENG. (a) and (b) FEM models of rotary-sliding disk TENGs: (a) dielectric-to-dielectric category, (b) conductor-to-dielectric category, including the contact and non-contact modes. (c) Typical electric potential distributions for the dielectric-to-dielectric TENG with $N = 4$ at various rotation angles: (1) 0°, (2) 30°, (3) 42°, (4) 45°. (d) Short-circuit charge, open-circuit voltage, and capacitance as functions of rotation angle for two categories of TENGs.

Table 1 Parameters utilized in the FEM calculation for the RD-TENG

Dielectric 1	$\varepsilon_{r1} = 4$, $d_1 = 100$ μm
Dielectric 2	$\varepsilon_{r2} = 2$, $d_2 = 100$ μm
Inner radius r_1 of TENG	5 mm
Outer radius r_2 of TENG	50 mm
Tribo-charge surface density σ	10 μC/m^2
Grating number N	1 ~ 8
Center angle of grating unit θ_0	$\theta_0 = \pi/N$
Angle velocity ω of rotation	20π rad/s

the $Q_{initial}$ was assigned to the total amount of charges transferred at $\alpha = 0$ under the SC condition for the non-contact mode. The SC transferred charges (Q_{SC}) was obtained by deducting $Q_{initial}$ from the total transferred charges under SC ($Q_{net,SC}$) at a certain angle α.

The charge reference state (SC state at $\alpha = 0$) was chosen to facilitate the theoretical calculations, similar to our previous work [22]. Subsequently, the OC voltage V_{OC} for various α was calculated by assigning the total charges of metal 1 and metal 2 to $-Q_{initial}$ and $Q_{initial}$. The electrodes made of metal are equipotential bodies. That is, all regions in one electrode have the same electric potential. To obtain the value of V_{OC}, we simply need to pick up the value of electric potential at one point of the electrode in the FEM simulation. The difference of electric potential between two electrodes is V_{OC}. The capacitance C was extracted by the linear interpolation method from the V–Q–α relation [23, 24]. For the metal RD-TENG, the boundary conditions and simulation method are similar.

Figure 1(c) shows the typical electric potential distributions at various rotation angles for dielectric

RD-TENG with $N = 4$ working in contact mode. From the half-cycle result, at $\alpha = 0$, there is no electric potential difference between the two electrodes. With increasing α, the potential difference gradually increases (V_{OC} increases as shown in Fig. 1(d)), and becomes sharp when α approaches θ_0 (45°). The sharp increase of V_{OC} is due to the severe edge effect. A maximum potential difference of ~2,200 V is generated when two dielectric layers are fully separated ($\alpha = \theta_0$). Q_{SC}, V_{OC}, and C at various α for the dielectric RD-TENG and metal RD-TENG in contact mode were also compared, as presented in Fig. 1(d). It can be seen that Q_{SC} increases linearly with α at $0 \leqslant \alpha \leqslant \theta_0$ and decreases linearly at $\theta_0 \leqslant \alpha \leqslant 2\theta_0$. The Q_{SC} curves for two TENGs are almost overlapping, implying that the Q_{SC} is independent of the triboelectric materials, which is in accordance with the theoretical equation of Q_{SC}. The Q_{SC}–α equation, derived by ideal charge distribution under the SC condition, is given by

$$Q_{SC} = \begin{cases} \dfrac{N\sigma\alpha(r_2^{\,2} - r_1^{\,2})}{2}, & 0 \leqslant \alpha \leqslant \theta_0 \\[2mm] N\sigma\left(\theta_0 - \dfrac{\alpha}{2}\right)(r_2^{\,2} - r_1^{\,2}), & \theta_0 \leqslant \alpha \leqslant 2\theta_0 \end{cases} \quad (1)$$

V_{OC} of the dielectric RD-TENG is higher than that of the metal RD-TENG, because of the lower capacitance. The capacitance curve is roughly linear and has a slight non-linearity around the half-cycle region. As long as two dielectrics are not fully separated, the capacitance C can be estimated according to the parallel-plate capacitor model, given by

$$C = \frac{N\varepsilon_0 \left|\theta_0 - \alpha\right| \cdot (r_2^{\,2} - r_1^{\,2})}{2\left(\dfrac{d_1}{\varepsilon_{r1}} + \dfrac{d_2}{\varepsilon_{r2}}\right)} \quad (2)$$

where ε_0 represents the vacuum permittivity. For metal RD-TENG, d_1 is set to 0 in Eq. (2).

We know that the change of potential difference between electrodes caused by periodic charge separation drives the current flowing through the external circuit during the rotation. That is the basic working mechanism of the RD-TENG. The basic output properties of the TENG can be directly impacted by the TENG structural parameters, such as the tribo-surface spacing h, grating number N, and geometric size. That is important for the optimal design of nanogenerators, and needs to be systematically discussed.

2.1 Effect of tribo-surface spacing

The tribo-surface spacing h determines whether the working mode is contact or non-contact. In the non-contact mode, dielectric 1 and dielectric 2 should be in contact first so that the two surfaces are charged positively and negatively, respectively, because of the triboelectrification process. Then, the two surfaces are separated by spacing h. When the dielectric 1 layer rotates in parallel with dielectric 2 for an angle, the free electrons in the bottom electrode will flow to the top electrode to balance/screen the non-mobile tribo-charges at the lower surface of dielectric 1. When the dielectric 1 layer continues to rotate and starts to overlap with the next dielectric 2 layer on another segment, the free electrons in the top electrode will flow back to the bottom electrode. This is the working mechanism of the non-contact mode. In our simulation, we assigned the surface charge density to two dielectric films, and these charges are generated by the contact before the rotation motion. To demonstrate the difference of the two modes, we studied the influence of the h value on the basic property qualities of TENG. The typical results for the dielectric RD-TENG with $N = 4$ are shown in Fig. 2. It can be found that Q_{SC}, C, and V_{OC} all have mirror symmetry in one cycle for the assigned h values. Q_{SC} and C both consist of two approximately linear lines, and V_{OC} changes sharply around the half-cycle ($T/2$) point. The three qualities all reach their extreme values at the $T/2$ point. Then, the effect of h can be seen. As the tribo-surface spacing increases, Q_{SC}, C, and V_{OC} all decrease markedly. At the $T/2$ point, the capacitance C decreases from 17.253 to 10.627 pF when increasing the h value from 0 to 1 mm. Note that the rotating-induced transferred charge change under the SC condition barely depends on the chosen charge reference state; however, the V_{OC} curve is greatly affected (Fig. S1 in the Electronic Supplementary Material (ESM), real short-circuit charge and open-circuit voltage). In addition, the case of metal RD-TENG was also investigated, whose results indicate that the trends of three basic parameters are similar
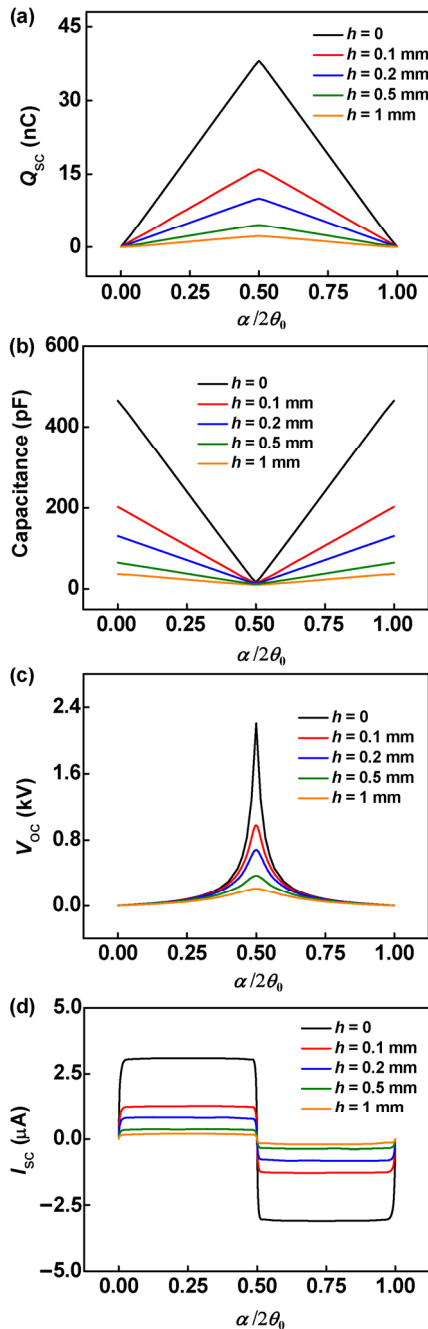
Figure 2 Effect of tribo-surface spacing on the basic properties of TENG: (a) short-circuit charge Q_{SC}, (b) capacitance C, (c) open-circuit voltage V_{OC}, and (d) short-circuit current I_{SC} as functions of rotation angle for the dielectric RD-TENG at various tribo-surface spacings h under the charge reference state.

to the dielectric RD-TENG, but the metal type has a higher capacitance, lower OC voltage, and lower SC charge (Fig. S2 in the ESM).

From the FEM results, we can also calculate the short-circuit current (I_{SC}) of dielectric RD-TENG with an

assumed specific motion mode. When the top rotator is assumed to rotate at a constant angular velocity ω (20π rad/s), the I_{SC} curves were obtained through the differentiation of Q_{SC} in Fig. 2(a). As expected, the I_{SC} has a constant value for each h value, which is reduced by the increase in h (Fig. 2(d)). The non-contact mode TENG exhibits a lower SC current than the contact mode TENG; nevertheless, the non-contact of two materials can avoid producing heat loss and reduce material wear, thereby facilitating its wide application in self-powered systems.

To better demonstrate the dependence of basic properties on h, we derived analytic equations for Q_{SC}, C, and V_{OC} for the ideal case (neglecting the edge effect). On the basis of the ideal charge distribution under SC condition and zero electric field inside metal, Q_{SC} can be given by

$$Q_{SC} = \begin{cases} \dfrac{N\sigma\alpha\left(\dfrac{d_1}{\varepsilon_{r1}} + \dfrac{d_2}{\varepsilon_{r2}}\right)(r_2^2 - r_1^2)}{2\left(\dfrac{d_1}{\varepsilon_{r1}} + \dfrac{d_2}{\varepsilon_{r2}} + h\right)}, & 0 \leqslant \alpha \leqslant \theta_0 \\[2em] \dfrac{N\sigma(2\theta_0 - \alpha)\left(\dfrac{d_1}{\varepsilon_{r1}} + \dfrac{d_2}{\varepsilon_{r2}}\right)(r_2^2 - r_1^2)}{2\left(\dfrac{d_1}{\varepsilon_{r1}} + \dfrac{d_2}{\varepsilon_{r2}} + h\right)}, & \theta_0 \leqslant \alpha \leqslant 2\theta_0 \end{cases}$$

(3)

When two dielectrics are not close to fully separated, the total capacitance C can be estimated by

$$C = \frac{N\varepsilon_0 |\theta_0 - \alpha| \cdot (r_2^2 - r_1^2)}{2\left(\dfrac{d_1}{\varepsilon_{r1}} + \dfrac{d_2}{\varepsilon_{r2}} + h\right)}$$

(4)

Then, the open-circuit voltage can be obtained by

$$V_{OC} = \begin{cases} \dfrac{\sigma\alpha}{\varepsilon_0(\theta_0 - \alpha)}\left(\dfrac{d_1}{\varepsilon_{r1}} + \dfrac{d_2}{\varepsilon_{r2}}\right), & 0 \leqslant \alpha < \theta_0 \\[1.5em] \dfrac{\sigma(2\theta_0 - \alpha)}{\varepsilon_0(\alpha - \theta_0)}\left(\dfrac{d_1}{\varepsilon_{r1}} + \dfrac{d_2}{\varepsilon_{r2}}\right), & \theta_0 < \alpha \leqslant 2\theta_0 \end{cases}$$

(5)

The detailed derivation can be found in section S1 of the ESM. From Eqs. (3) and (4), we can see the Q_{SC} and C both decrease with increasing h, agreeing with

the FEM simulations. From Eq. (5), the ideal V_{OC} is independent of h, but it is not suitable for the half-cycle region, because the edge effect is severe.

Regarding the efficiency of the nanogenerator, there are two types of efficiency, i.e., charge transfer efficiency and energy conversion efficiency. The charge transfer efficiency under the SC condition η_{SC} is defined as Q_{SC}/Q_{tribo} (Q_{tribo} is total tribo-charge amount). From Fig. 2(a), we know the Q_{SC} of the non-contact mode is lower than that of the contact mode, so the η_{SC} of the non-contact mode is relatively lower for a fixed Q_{tribo}, reflecting a lower charge transfer capacity. For the energy conversion, the non-contact mode can largely reduce the heat energy loss and has higher energy conversion efficiency than the contact mode.

To verify the theoretical results, we carried out experiments for the RD-TENG applying the triboelectrification between Al and polytetrafluoroethylene (PTFE). The voltage and current were measured by a Keithley 6514 electrometer and a Stanford low-noise current preamplifier (Model SR570), respectively. The current I_{SC} profile of the TENG without rectification for $h = 0$ at a rotation rate of 275 r/min is shown in Fig. 3(a). It

can be seen that at such a low rotation rate, the I_{SC} curve approximately exhibits a square wave, similar to the theoretical result. Then, we measured the open-circuit voltage V_{OC} and short-circuit current density J_{SC} of the TENG with rectification for $h = 0$ at a high rotation rate of 900 r/min, which are shown in Figs. 3(b) and 3(c). A maximum voltage of 580 V and a maximum current density of 45 mA/m² were obtained. The relationships between the voltage, current density, and spacing h were plotted as shown in Figs. 3(d) and 3(e). The output signals present an approximately constant DC feature, because the charge transfer time in one cycle is extended notably when the capacitance of the rectifier bridge is comparable to the TENG capacitance for a non-zero h. The experimental measurements that voltage and current both decrease with increasing spacing h are consistent with the theoretical results. In addition, we should note that the experimental voltage and current curves show some distortions in comparison with our simulated results. This is due to the imperfect rotation condition and the electrostatic influences from the environment. However, the accordance in the changing tendency of output
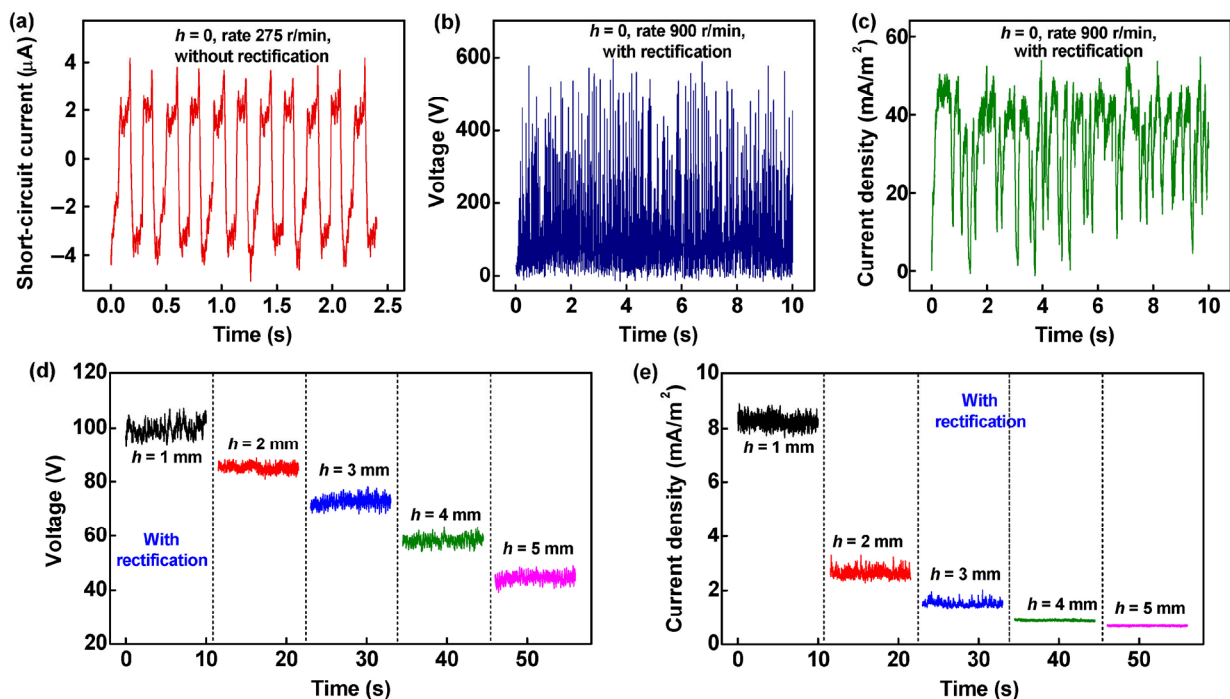
Figure 3 Experimental measurements of an RD-TENG applying the triboelectrification between Al and PTFE. (a) Short-circuit current I_{SC} profile without rectification for $h = 0$ at a rotation rate of 275 r/min. (b) Open-circuit voltage V_{OC} and (c) short-circuit current density J_{SC} as functions of time for the RD-TENG with rectification for $h = 0$ at a rotation rate of 900 r/min. (d) and (e) V_{OC} and J_{SC} profiles with respect to h for the RD-TENG with rectification at a rotation rate of 900 r/min.

performance with the structural parameter between experiments and simulations can confirm the validity of the theoretical analysis.

2.2 Effect of grating number

In addition to the spacing between two tribo-surfaces, the grating number N is another important design parameter of the RD-TENG. When N is small, the geometric size of the grating unit (arc length l of each unit) is much larger than the thickness (d_1 or d_2) of the dielectrics, so the edge effect can be neglected. Under this ideal condition, the relationship between Q_{SC}, C, and N can be theoretically given by Eqs. (1) and (2). The charge transfer efficiency η_{SC} can reach 100% at the half-cycle $T/2$. The accumulated charges ($Q_{SC\text{-rectified}}$) and charge transfer efficiency ($\eta_{SC\text{-rectified}}$) after rectification under SC when a rotation angle of π is finished

can be calculated by $N\pi\sigma(r_2^2 - r_1^2)/2$ and N. $Q_{SC\text{-rectified}}$ and $\eta_{SC\text{-rectified}}$ in the grating-disk structure can be enhanced by N times through the subdivision process under ideal conditions. However, when N is fairly large or l is comparable with d, the non-ideal edge effect is significant and cannot be ignored.

In order to validate the theoretical analysis for the ideal or non-ideal cases, we carried out FEM simulations for the dielectric RD-TENG under ideal conditions (L/d = 314.2, L denotes the circumference of the inner circle) and under non-ideal conditions (L/d = 6.3), respectively. The typical Q_{SC}, I_{SC}, C, and V_{OC} for the dielectric RD-TENG in contact mode with various N under ideal conditions are shown in Figs. 4(a)–4(d). As can be seen, Q_{SC} is almost unchanged by N, but the increase of N induces an increase in $Q_{SC\text{-rectified}}$. The calculated values of $Q_{SC\text{-rectified}}$ are proportional to N,
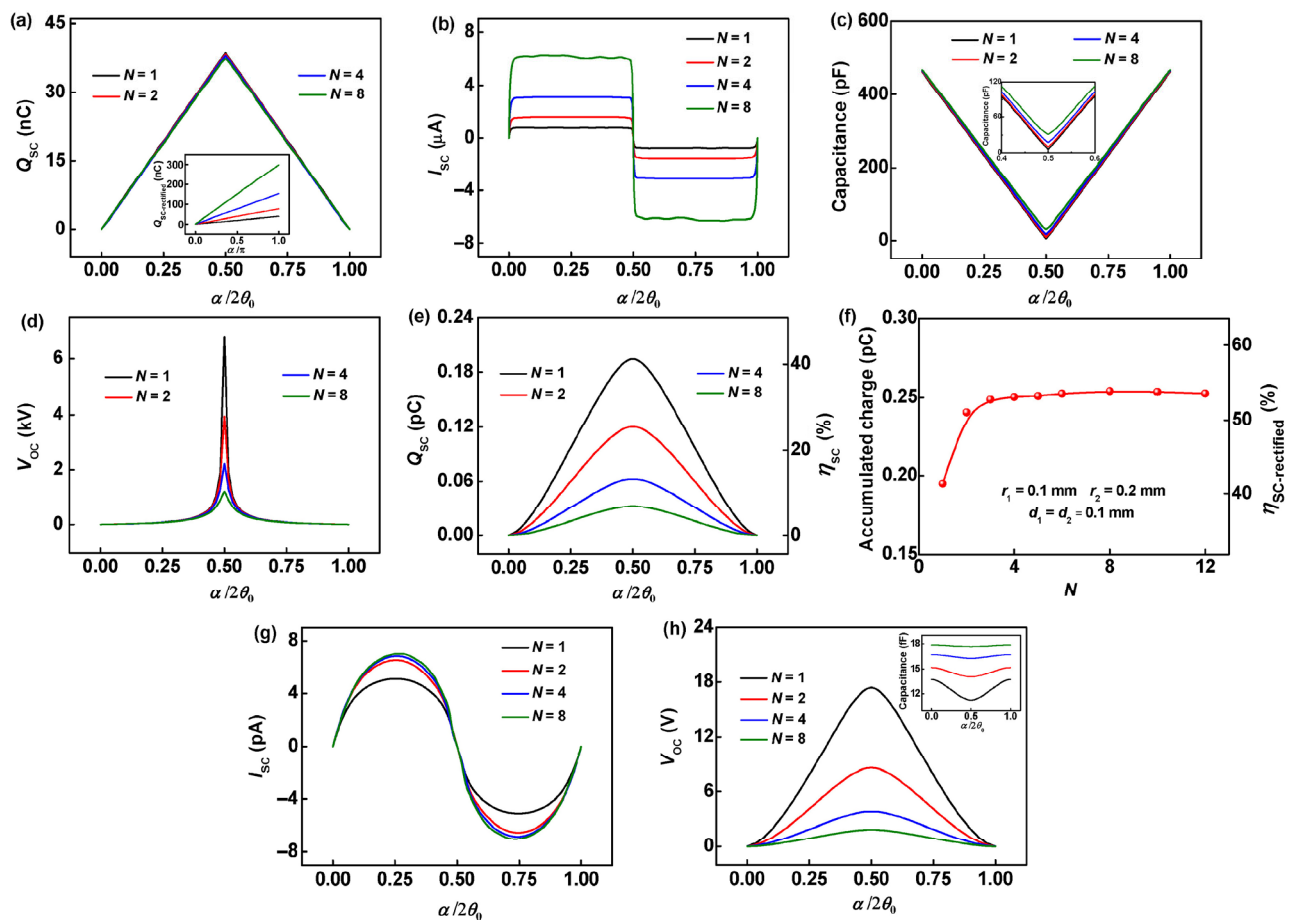
Figure 4 Effect of grating number on the basic TENG properties: (a) short-circuit charge, (b) short-circuit current, (c) capacitance, and (d) open-circuit voltage as functions of rotation angle for the dielectric RD-TENG with various grating numbers N under the ideal condition. (e) Q_{SC} and η_{SC} profiles of TENG with a small L/d ratio during one cycle at different N. (f) Total SC transferred charge and efficiency with respect to N when rotating for the angle of π. (g) I_{SC} profiles and (h) V_{OC} and C profiles of the TENG with a small L/d ratio for various N.

which is in good agreement with the theoretical analysis. I_{SC} has a constant value for each N value, and it increases with the increase of N (Fig. 4(b)). The maximum of V_{OC} significantly drops with increasing N from 1 to 8 (Fig. 4(d)), because a finer pitch brings a great increase in minimum capacitance from 5.679 to 30.843 pF (a factor of 5~6) when two dielectrics are fully separated (Fig. 4(c)). In addition, for a metal RD-TENG, the influence of grating number is similar under the ideal condition (see Fig. S5 in the ESM).

For the non-ideal case, we calculated the Q_{SC}, η_{SC}, I_{SC}, V_{OC}, and C for a grating dielectric RD-TENG with a small L/d ratio ($r_1 = 0.1$ mm, $r_2 = 0.2$ mm, and $d_1 = d_2 = 0.1$ mm) in one cycle, as presented in Figs. 4(e)–4(h). The Q_{SC} curves become non-linear, and the Q_{SC} and η_{SC} decrease significantly with increasing N, different from the ideal case. The maximum η_{SC} cannot arrive at 100% like in the ideal case; instead, it descends from 41.4% to 7.0%. That makes $Q_{SC\text{-rectified}}$ and $\eta_{SC\text{-rectified}}$ become saturated at a low grating number (Fig. 4(f)). The non-ideal effect also changes the curve shape of I_{SC}, V_{OC} and C. The I_{SC} has a sine-wave shape for any N, and it increases with the increase in N (Fig. 4(g)). However, the growth rate of I_{SC} decreases dramatically because of the non-ideal edge effect. The V_{OC} curve has the same shape as Q_{SC}, because of the small capacitance value (Fig. 4(h)). From the insert, the capacitance change is also not linear anymore. For the non-ideal case, the leakage electric field from the imperfect edge results in the interaction effect between two adjacent units, which can be called a small-edge effect. Accordingly, the sensitivity of potential variation in response to the geometrical changing of the TENG would be decreased significantly. Therefore, the linear changing of the V_{OC} and C during the rotation cannot be observed because of the delayed potential changing between two electrodes by the small-edge effect. In the ultimate stage, the potential distribution cannot obey the theory and the output voltage becomes zero. Therefore, the edge effect under specific conditions can have remarkable impacts on the basic properties of RD-TENG.
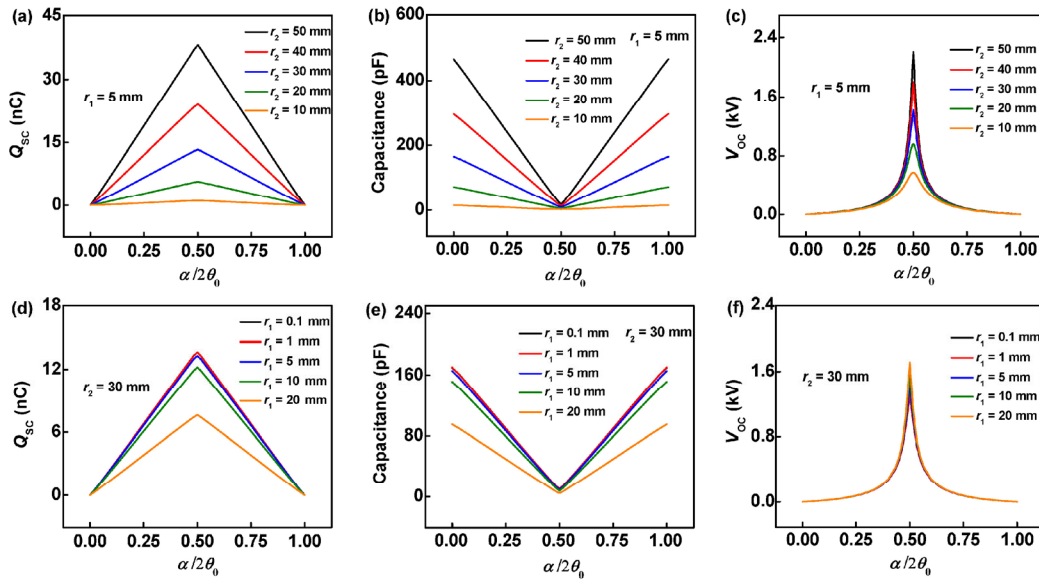
2.3   Effect of geometric size

The geometric size, including the inner radius r_1 and outer radius r_2, can determine the tribo-surface area and scale up the output. We performed a simulation

on the dieletric RD-TENG in contact mode through FEM calculation, in order to reveal the influence of geometric size. Q_{SC}, C, and V_{OC} of the RD-TENG with various r_2 when r_1 is fixed at 5 mm are shown in Figs. 5(a)–5(c). For any given α, a larger r_2 can generate a larger Q_{SC} because of the larger tribo-surface area and tribo-charges. According to the theoretical Eq. (1), Q_{SC} is proportional to the value of $(r_2^2 - r_1^2)$, but this is true only when r_2 is large enough, because the narrow lateral at a too-small r_2 can produce a non-negligible edge effect. The edge effect will lead to a decrease in charge transfer efficiency. Meanwhile, C and V_{OC} can both be raised by an increase in r_2. On the other hand, the results of the TENG with various r_1 at $r_2 = 30$ mm are presented in Figs. 5(d) and 5(e). It can be found that when r_1 is small, both Q_{SC} and C decrease slightly with increasing r_1, whereas they decrease significantly at large r_1. The decrease in Q_{SC} and C is ascribed to the smaller tribo-surface area at larger r_1. For V_{OC}, its peak value at the half-cycle point increases with the increase of r_1 resulting from the competition of decreases of Q_{SC} and C, but at other α regions it is almost unaffected by the change of r_1. The independence of V_{OC} on r_1 agrees with the theoretical equation of V_{OC}, which is the same as Eq. (5). The equation can be derived from Eqs. (1) and (2). In Eq. (1), the Q_{SC}–α equation is obtained from the ideal charge distribution under the SC condition. Q_{SC}, which equals the amount of tribo-charges at the non-overlapped region, is the total SC transferred charge under the ideal condition. In Eq. (2), the total capacitance C can be estimated by the capacitance at the overlapped region. Because the thickness of the dielectrics is much smaller than their length, the capacitor between the overlapped region is the dominant part of the total capacitance as long as the two dielectrics are not close to fully separated. By dividing total Q_{SC} by total C, we can obtain the ideal total V_{OC} (Eq. (5)). The above analysis regarding the size effect of the TENG can provide useful information for scaling up the output performance of an RD-TENG.

3   Dynamic output characteristics and optimization

To further understand the output characteristics of the RD-TENG, its governing equation (V–Q–α relationship)

Figure 5 Effect of geometric size on the basic TENG properties: (a) and (d) short-circuit charge, (b) and (e) capacitance, and (c) and (f) open-circuit voltage as functions of rotation angle for the dielectric RD-TENG with various r_2 and r_1 working in contact mode.

was systematically investigated. According to previous work [17, 25], at constant α, voltage output V and Q show an accurate linear curve, in which the slope is the negative reciprocal value of capacitance and the intercept of the V-axis is V_{OC}. Therefore, the V–Q–α relationship is given by

$$V = -\frac{1}{C(\alpha)} \times Q + V_{OC}(\alpha) \qquad (6)$$

When two tribo-surfaces are not close to fully separated or unmatched, the approximate analytical equation of $C(\alpha)$ can be found in Eq. (2), and then the analytical equation of $V_{OC}(\alpha)$ can be obtained by $V_{OC} = Q_{SC}/C$. However, when the rotator and stator have a full separation or mismatch, the analytical equations are not appropriate because of the edge effect. Because of the continuous rotation of the disk structure, approximate equations suited for the entire region of rotation angle are needed to reveal the output characteristics. Thus we utilized the continuous fraction interpolation to provide the approximate equations of $1/C(\alpha)$ and $V_{OC}(\alpha)$. The interpolation method equations are given by [26, 27]

$$\frac{1}{C(\alpha)} = m_0 + \cfrac{\alpha - \alpha_0}{m_1 + \cfrac{\alpha - \alpha_1}{m_2 + \cdots + \cfrac{\alpha - \alpha_{15}}{m_{16}}}} \qquad (7)$$

$$V_{OC}(\alpha) = n_0 + \cfrac{\alpha - \alpha_0}{n_1 + \cfrac{\alpha - \alpha_1}{n_2 + \cdots + \cfrac{\alpha - \alpha_{15}}{n_{16}}}} \qquad (8)$$

The $1/C$ and V_{OC} at different α can be extracted by the linear interpolation of the FEM results, and the typical results of dielectric RD-TENG in contact mode are listed in Table S1 of the ESM. The values of the interpolation parameters are listed in Table S2 (in the ESM). We also compared the interpolation results and FEM results and a good agreement was achieved (Fig. S6 in the ESM). By merging the interpolation parameters into Eqs. (7), (8) and substituting Eqs. (7), (8) into Eq. (6), an approximate semi-analytical V–Q–α relationship was obtained.

3.1 Resistive load output characteristics

The resistive load characteristics can be calculated by combining the semi-analytical V–Q–α relationship and Ohm's law through the following equation

$$R\frac{dQ}{dt} = V = -\frac{1}{C(\alpha)} \times Q + V_{OC}(\alpha) \qquad (9)$$

The differential equation can be solved by specifying the motion process (specified $\alpha(t)$ profile) and the boundary condition. We chose a constant angle velocity

rotation for the motion process as a typical example. The α–t relationship for constant ω is mathematically given by

$$\alpha(t) = \omega t \qquad (10)$$

Because the disk structure and rotation process is periodic, output from any initial boundary condition will gradually converge to a periodic output wave with the same period after the first few periods [23, 24]. By applying the periodic boundary condition

$$Q(t = 0) = Q\left(t = \frac{2\theta_0}{\omega}\right) \qquad (11)$$

the steady-state output of the RD-TENG for arbitrary load resistance can be calculated. The equations for transferred charge Q are obtained as follows

$$Q = \exp\left(-\int_0^t \frac{\mathrm{d}t}{C(\omega t)R}\right)$$
$$\times\left[Q_0 + \int_0^t \frac{V_{\mathrm{OC}}(\omega t)}{R}\exp\left(\int_0^t \frac{\mathrm{d}z}{C(\omega z)R}\right)\mathrm{d}t\right], \quad 0 \leqslant t \leqslant \frac{\theta_0}{\omega}$$
$$(12\mathrm{a})$$

$$Q = \exp\left(-\int_{\frac{\theta_0}{\omega}}^t \frac{\mathrm{d}t}{C(\omega t)R}\right)$$
$$\times\left[Q\left(\frac{\theta_0}{\omega}\right) + \int_{\frac{\theta_0}{\omega}}^t \frac{V_{\mathrm{OC}}(\omega t)}{R}\exp\left(\int_{\frac{\theta_0}{\omega}}^t \frac{\mathrm{d}z}{C(\omega z)R}\right)\mathrm{d}t\right],$$
$$\frac{\theta_0}{\omega} \leqslant t \leqslant \frac{2\theta_0}{\omega}$$
$$(12\mathrm{b})$$

where Q_0 is given by

$$Q_0 = Q(t = 0) = \frac{\exp\left(-\frac{2}{R\omega}\int_0^{\theta_0} \frac{\mathrm{d}\alpha}{C(\alpha)}\right)}{1 - \exp\left(-\frac{2}{R\omega}\int_0^{\theta_0} \frac{\mathrm{d}\alpha}{C(\alpha)}\right)}$$
$$\times \frac{1}{R\omega}\int_0^{\theta_0} V_{\mathrm{OC}}(\alpha)\exp\left(\frac{1}{R\omega}\int_0^{\alpha} \frac{\mathrm{d}z}{C(z)}\right)\mathrm{d}\alpha \qquad (13)$$
$$+ \frac{1}{1 - \exp\left(-\frac{2}{R\omega}\int_0^{\theta_0} \frac{\mathrm{d}\alpha}{C(\alpha)}\right)}$$
$$\times \frac{1}{R\omega}\int_0^{\theta_0} V_{\mathrm{OC}}(\alpha)\exp\left(-\frac{1}{R\omega}\int_0^{\alpha} \frac{\mathrm{d}z}{C(z)}\right)\mathrm{d}\alpha$$

Through the differentiation of Q by t, we can obtain the equations of current I for arbitrary load resistance

$$I = \frac{V_{\mathrm{OC}}(\omega t)}{R} - \frac{\exp\left(-\int_0^t \frac{\mathrm{d}t}{C(\omega t)R}\right)}{C(\omega t)R}$$
$$\times\left[Q_0 + \int_0^t \frac{V_{\mathrm{OC}}(\omega t)}{R}\exp\left(\int_0^t \frac{\mathrm{d}z}{C(\omega z)R}\right)\mathrm{d}t\right], \quad 0 \leqslant t \leqslant \frac{\theta_0}{\omega}$$
$$(14\mathrm{a})$$

$$I = \frac{V_{\mathrm{OC}}(\omega t)}{R} - \frac{\exp\left(-\int_{\frac{\theta_0}{\omega}}^t \frac{\mathrm{d}t}{C(\omega t)R}\right)}{C(\omega t)R}$$
$$\times\left[Q\left(\frac{\theta_0}{\omega}\right) + \int_{\frac{\theta_0}{\omega}}^t \frac{V_{\mathrm{OC}}(\omega t)}{R}\exp\left(\int_{\frac{\theta_0}{\omega}}^t \frac{\mathrm{d}z}{C(\omega z)R}\right)\mathrm{d}t\right],$$
$$\frac{\theta_0}{\omega} \leqslant t \leqslant \frac{2\theta_0}{\omega}$$
$$(14\mathrm{b})$$

Then, the voltage V can be calculated by Ohm's law. For a more detailed derivation, see the ESM, section S4.

Numerical calculations of the real-time output characteristics of a dielectric RD-TENG working in contact mode at different load resistances for $N = 4$ and $\omega = 20\pi$ rad/s are presented in Fig. 6. The parameters utilized in the calculations are the same as those shown in Table 1. Only one-cycle results at various resistances R for Q, I, and V are shown, because the Q–t, I–t, and V–t curves are periodic waves with a period of $2\theta_0/\omega$. At small R (<1 MΩ), the limitation effect of charge transfer of the resistor is small and the charge and current curves are close to the SC curves. The charge linearly changes, and the current exhibits a square wave. As R increases, the oscillation magnitude of the Q curve decreases gradually to 0 (Fig. 6(a)), because the charge transport becomes more and more limited. The current and voltage are both alternating-current signals, and their integrations in one cycle are both zero because of the periodic structure of the disk TENG. With increasing R, the positive peak of I increases first, and then decreases to approximately 0 at a sufficiently large R (Fig. 6(b)). The increase in the I peak may be attributed to the competition of the increasing speed of the V peak and resistance. Meanwhile, the voltage curve converges towards the OC curve, and its positive peak rises gradually as shown in Fig. 6(c).
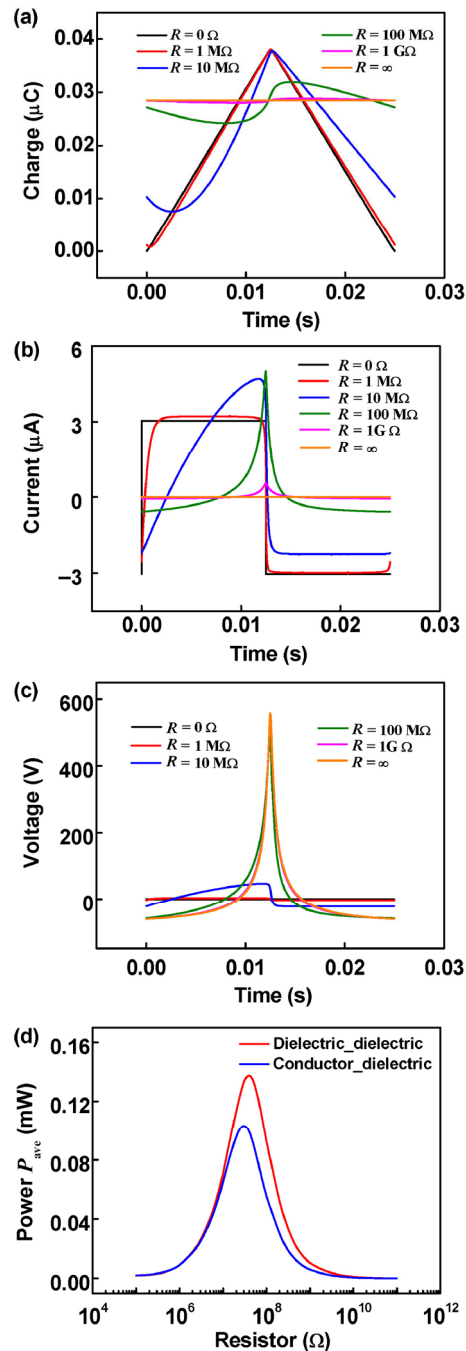
Figure 6 Output characteristics for the dielectric RD-TENG during one cycle with grating number $N = 4$: (a) transferred charge-time relationship at different load resistances, (b) current–time relationship at different load resistances, and (c) voltage–time relationship at different load resistances. (d) Comparison of average output power as a function of resistance for two kinds of TENGs.

From this analysis, the RD-TENG also shows a three-working-region behavior inducing an optimized output, because of the impedance match between the inherent capacitance of the TENG and load resistance. Then,

we used the average output power P_{ave} to characterize the output performance of this TENG, where P_{ave} was defined by

$$P_{ave} = \frac{\int_0^T I^2 R \, dt}{T}, \quad T = \frac{2\theta_0}{\omega} \tag{15}$$

P_{ave} as a function of R was compared in Fig. 6(d) for the dielectric and metal RD-TENG in contact mode ($N = 4$, $\omega = 20\pi$ rad/s). For both categories of TENG, an optimum resistance is observed for the average power to reach its maximum. Through a comparison, we can find that the dielectric RD-TENG generates higher average output power at a higher optimum resistance relative to the metal RD-TENG, which may serve as important guidance for rational design of the TENG structure in specific applications. The higher optimum resistance of the dielectric RD-TENG is because of its smaller capacitance.

3.2 Influencing factors of output performance and power optimization

In this subsection, we explore the influences of structural parameters and rotation rate on the load output performance of the RD-TENG, reflected by the average output power P_{ave}. Figure 7 shows the calculated P_{ave} as a function of resistance R at various tribo-surface spacings ($N = 4$, $\omega = 20\pi$ rad/s), grating numbers ($h = 0$, $\omega = 20\pi$ rad/s), and rotation rates ($N = 4$, $h = 0$). From Fig. 7(a), we can find that for the dielectric RD-TENG, as the spacing h increases, the power at a constant R gradually decreases, accompanied by the shift of optimum resistance (the resistance at maximum P_{ave}) to higher values. The decrease of power is closely related to the decreases of I_{SC} and V_{OC} (Figs. 2(c) and 2(d)). The relationships between optimum power (peak value of P_{ave}), optimum resistance, and h can also be seen in Fig. 7(b). Figure 7(b) clearly indicates that the optimum power decreases while the optimum resistance increases with increasing h for two RD-TENGs. Although the same variation trends of optimum power and resistance are found for two types of TENGs, the dielectric RD-TENG has higher optimum power and matched resistance arising from its higher I_{SC} and V_{OC}, and lower C (Fig. 1).
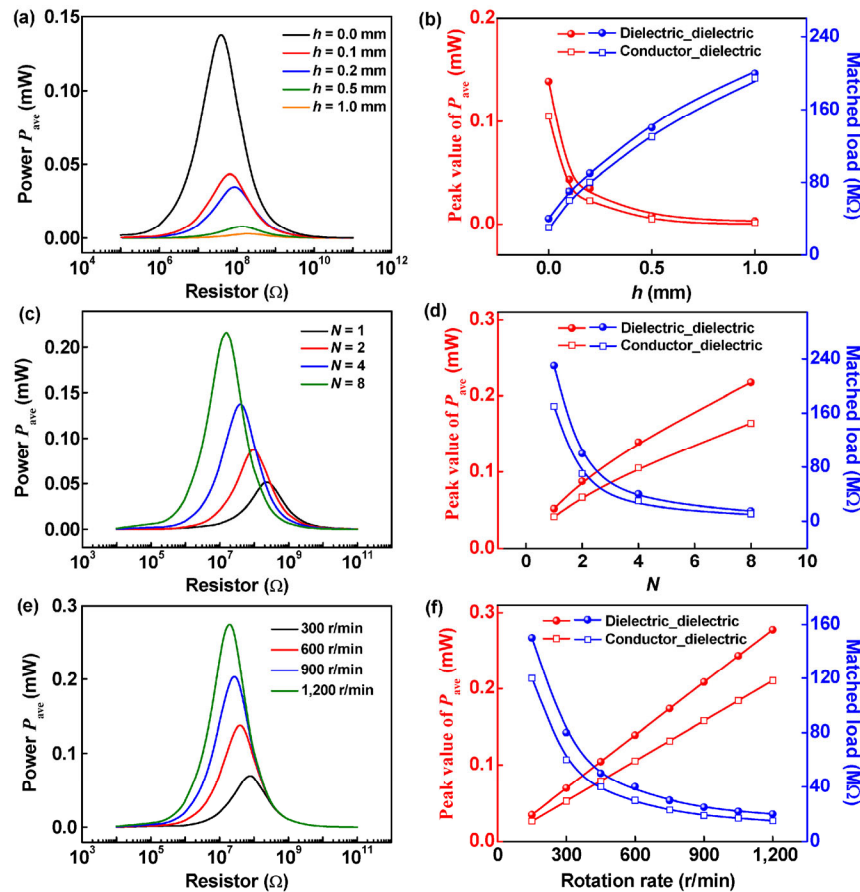
Figure 7 (a), (c), and (e) Average power as a function of resistance for the dielectric RD-TENG at various (a) tribo-surface spacings h, (c) grating numbers N, and (e) rotation rates w. (b), (d), and (f) Dependencies of P_{ave} peak and matched load on (b) h, (d) N, and (f) w for two categories of RD-TENGs.

The numerical results of output power and matched load resistance for various grating numbers are shown in Figs. 7(c) and 7(d). This indicates that the dielectric RD-TENG delivers higher optimum power at a lower optimum resistance for a larger N. In the low-resistance range, the output power at a constant R increases with the increase of N, whereas it decreases in the higher resistance range. That is because the power is respectively dominated by I_{SC} and V_{OC} in the two resistance regions. Meanwhile, the metal RD-TENG generates lower optimum power and resistance at various N than the dielectric RD-TENG (Fig. 7(d)). When N increases in the small region, the average value of I_{SC} increases more significantly than V_{OC} decreases, so the average power will increase. However, when N continues to increase, the growth rate of I_{SC} decreases dramatically because of the non-ideal edge effect. Furthermore, the average power will start to decrease when the

decreasing V_{OC} becomes the dominant factor. Therefore, there exists an optimum N to maximize the average output power. The detailed results can be found in our previous work [22], in which an optimum grating number of approximately 100 was obtained for the sliding TENG through a 2D model. In this work, because of the limitation of extreme computation costs on the 3D model, the load performance of the RD-TENG was addressed only under ideal conditions (small N).

For the influence of rotation rate, when the rotation rate increases, the output power increases gradually, and the matched resistance shifts towards a lower R (Fig. 7(e)). The increase of optimum power exhibits a linear character (Fig. 7(f)). The comparison of a dielectric RD-TENG and a metal one was also made in Fig. 7(f), and similar regularity was found. As discussed above, the optimum power of RD-TENG on load resistance

relies on the OC and SC output property, and the matched resistance is dependent on the capacitance and angular velocity. The optimum resistance can be thought of as the "impedance" match between C and the load resistance; therefore, such trends of optimum resistance can further validate that the impedance of TENG can be expressed by $1/\omega C$. On the other hand, the RD-TENG device can be considered as a capacitor with periodic capacitance values, and this capacitor undergoes repetitive charging and discharging processes during the rotation of the RD-TENG. In this respect, the circuit time constant of a TENG with a load resistance is given by $\tau = RC$, which needs to match with the time period ($2\theta_0/\omega$) of rotation, in order to achieve the optimized output power. Hence, at a fixed N (the changing of C is the same), the smaller rotation period at a larger rotation rate needs to match with a smaller τ, and the resistance R shifts to a lower value as shown in Fig. 7(e). Meanwhile, the increase of N could lead to an increase in average capacitance and a decrease in time period. As a result, the load resistance needs to be decreased to maintain a smaller τ (Fig. 7(c)). It is also important to note that the increasing rotation period makes the energy transfer more efficient and elevates the maximum output power (Figs. 7(e) and 7(f)).

4   Conclusion

In summary, a theoretical model of the rotary-sliding disk TENG was presented, which includes the dielectric and metal RD-TENGs working in both contact and non-contact modes. FEM analysis was utilized to systematically characterize Q_{SC}, C, and V_{OC} of the RD-TENG, and their strong dependencies on the triboelectric material and structural parameters were discovered. From the FEM calculations, approximate semi-analytical V–Q–α equations were obtained by the continuous fraction interpolation method. Furthermore, by numerically solving the semi-analytical equation, the resistive load output characteristics of the RD-TENG were investigated. Finally, the relationships of average output power, optimum resistance and tribo-surface spacing, grating number, and rotation rate were revealed. The discussion of the influences of structural parameters and operating conditions on

the whole performance of the device can provide useful guidance for rational design of the device structure towards the optimum output in self-powered system applications.

References

[1]   O'Regan, B.; Grätzel, M. A low-cost, high-efficiency solar cell based on dye-sensitized colloidal TiO$_2$ films. *Nature* **1991**, *353*, 737–740.

[2]   Dresselhaus, M. S.; Chen, G.; Tang, M. Y.; Yang, R. G.; Lee, H.; Wang, D. Z.; Ren, Z. F.; Fleurial, J. P.; Gogna, P. New directions for low-dimensional thermoelectric materials. *Adv. Mater.* **2007**, *19*, 1043–1053.

[3]   Wang, Z. L.; Zhu, G.; Yang, Y.; Wang, S. H.; Pan, C. F. Progress in nanogenerators for portable electronics. *Mater. Today* **2012**, *15*, 532–543.

[4]   Wang, S. H.; Lin, L.; Wang, Z. L. Triboelectric nanogenerators as self-powered active sensors. *Nano Energy* **2015**, *11*, 436–462.

[5]   Wang, Z. L.; Song, J. H. Piezoelectric nanogenerators based on zinc oxidenanowire arrays. *Science* **2006**, *312*, 242–246.

[6]   Qin, Y.; Wang, X. D.; Wang, Z. L. Microfibre–nanowire hybrid structure for energy scavenging. *Nature* **2008**, *451*, 809–813.

[7]   Williams, C. B.; Shearwood, C.; Harradine, M. A.; Mellor, P. H.; Birch, T. S.; Yates, R. B. Development of an electromagnetic micro-generator. *IEEE Proc. Circ. Dev. Syst.* **2001**, *148*, 337–342.

[8] Beeby, S. P.; Torah, R. N.; Tudor, M. J.; Glynne-Jones, P.; O'Donnell, T.; Saha, C. R.; Roy, S. A micro electromagnetic generator for vibration energy harvesting. *J. Micromech. Microeng.* **2007**, *17*, 1257–1265.

[9] Jefimenko, O. D.; Walker, D. K. Electrostatic current generator having a disk electret as an active element. *IEEE Trans. Ind. Appl.* **1978**, *IA-14*, 537–540.

[10] Basset, P.; Galayko, D.; Paracha, A. M.; Marty, F.; Dudka, A.; Bourouina, T. A batch-fabricated and electret-free silicon electrostatic vibration energy harvester. *J. Micromech. Microeng.* **2009**, *19*, 115025.

[11] Fan, F. R.; Tian, Z. Q.; Wang, Z. L. Flexible triboelectric generator. *Nano Energy* **2012**, *1*, 328–334.

[12] Yang, Y.; Zhang, H.; Chen, J.; Jing, Q. S.; Zhou, Y. S.; Wen, X. N.; Wang, Z. L. Single-electrode-based sliding triboelectric nanogenerator for self-powered displacement vector sensor system. *ACS Nano* **2013**, *7*, 7342–7351.

[13] Chen, X. Y.; Iwamoto, M.; Shi, Z. M.; Zhang, L. M.; Wang, Z. L. Self-powered trace memorization by conjunction of contact-electrification and ferroelectricity. *Adv. Funct. Mater.* **2015**, *25*, 739–746.

[14] Su, Y. J.; Wen, X. N.; Zhu, G.; Yang, J.; Chen, J.; Bai, P.; Wu, Z. M.; Jiang, Y. D.; Wang, Z. L. Hybrid triboelectric nanogenerator for harvesting water wave energy and as a self-powered distress signal emitter. *Nano Energy* **2014**, *9*, 186–195.

[15] Zhu, G.; Zhou, Y. S.; Bai, P.; Meng, X. S.; Jing, Q. S.; Chen, J.; Wang, Z. L. A shape-adaptive thin-film-based approach for 50% high-efficiency energy generation through micro-grating sliding electrification. *Adv. Mater.* **2014**, *26*, 3788–3796.

[16] Tang, W.; Jiang, T.; Fan, F. R.; Yu, A. F.; Zhang, C.; Cao, X.; Wang, Z. L. Liquid-metal electrode for high-performance triboelectric nanogenerator at an instantaneous energy conversion efficiency of 70.6%. *Adv. Funct. Mater.* **2015**, *25*, 3718–3725.

[17] Niu, S. M.; Liu, Y.; Wang, S. H.; Lin, L.; Zhou, Y. S.; Hu, Y. F.; Wang, Z. L. Theory of sliding-mode triboelectric nanogenerators. *Adv. Mater.* **2013**, *25*, 6184–6193.

[18] Wang, S. H.; Lin, L.; Xie, Y. N.; Jing, Q. S.; Niu, S. M.; Wang, Z. L. Sliding-triboelectric nanogenerators based on in-plane charge-separation mechanism. *Nano Lett.* **2013**, *13*, 2226–2233.

[19] Lin, L.; Wang, S. H.; Xie, Y. N.; Jing, Q. S.; Niu, S. M.; Hu, Y. F.; Wang, Z. L. Segmentally structured disk triboelectric nanogenerator for harvesting rotational mechanical energy. *Nano Lett.* **2013**, *13*, 2916–2923.

[20] Han, C. B.; Du, W. M.; Zhang, C.; Tang, W.; Zhang, L. M.; Wang, Z. L. Harvesting energy from automobile brake in contact and non-contact mode by conjunction of tribo-electrication and electrostatic-induction processes. *Nano Energy* **2014**, *6*, 59–65.

[21] Zhang, C.; Zhou, T.; Tang, W.; Han, C. B.; Zhang, L. M.; Wang, Z. L. Rotating-disk-based direct-current triboelectric nanogenerator. *Adv. Energy Mater.* **2014**, *4*, 1301798.

[22] Niu, S. M.; Wang, S. H.; Liu, Y.; Zhou, Y. S.; Lin, L.; Hu, Y. F.; Pradel, K. C.; Wang, Z. L. A theoretical study of grating structured triboelectric nanogenerators. *Energy Environ. Sci.* **2014**, *7*, 2339–2349.

[23] Jiang, T.; Chen, X. Y.; Han, C. B.; Tang, W.; Wang, Z. L. Theoretical study of rotary freestanding triboelectric nano-generators. *Adv. Funct. Mater.* **2015**, *25*, 2928–2938.

[24] Niu, S. M.; Liu, Y.; Chen, X. Y.; Wang, S. H.; Zhou, Y. S.; Lin, L.; Xie, Y. N.; Wang, Z. L. Theory of freestanding triboelectric-layer-based nanogenerators. *Nano Energy* **2015**, *12*, 760–774.

[25] Niu, S. M.; Zhou, Y. S.; Wang, S. H.; Liu, Y.; Lin, L.; Bando, Y.; Wang, Z. L. Simulation method for optimizing the performance of an integrated triboelectric nanogenerator energy harvesting system. *Nano Energy* **2014**, *8*, 150–156.

[26] Stoer, J.; Bulirsch, R. *Introduction to Numerical Analysis*; Springer: New York, 2002.

[27] Niu, S. M.; Liu, Y.; Wang, S. H.; Lin, L.; Zhou, Y. S.; Hu, Y. F.; Wang, Z. L. Theoretical investigation and structural optimization of single-electrode triboelectric nanogenerators. *Adv. Funct. Mater.* **2014**, *24*, 3332–3340.